Embryonic Durotaxis: A Mechanical Framework for Understanding Cesarean Scar Pregnancy

Jialing Cao[1, 6], Huanyu You[2, 6], Jianwen Li[1, 6], Shiping Yue[1], Bingqi Song[1], Hangyu Li[3], Jiyu Wei[2], Dongshi Guan[3,5], Yan Zu[4], Zheng Xu[3]*, Yan Wang[2]*, Yubo Fan[1]*, and Jing Du[1]*

[1]Beijing Advanced Innovation Center for Biomedical Engineering, School of Biological Science and Medical Engineering, Beihang University; Beijing, 100191, China

[2]Department of Obstetrics and Gynecology, Peking University Third Hospital, Beijing 100191, China

[3]State Key Laboratory of Nonlinear Mechanics, Institute of Mechanics, Chinese Academy of Sciences, Beijing 100190, China

[4]Wenzhou Institute, University of Chinese Academy of Sciences, Wenzhou, Zhejiang 325001, China

[5]School of Engineering Science, University of Chinese Academy of Sciences, Beijing 100049, China.

[6]These authors contributed equally

*Corresponding author. Email: Correspondence: wjgqhn@263.net (Y.W.), yubofan@buaa.edu.cn (YB.F.), dujing@buaa.edu.cn (J.D.)

Key words: cesarean scar pregnancy; durotaxis; substrate stiffness; embryo migration; implantation

ABSTRACT

Cesarean scar pregnancy (CSP), a serious complication associated with the global surge in cesarean sections, has been a significant rise in prevalence. However, the pathogenic mechanisms driving CSP remain poorly understood. In this study, we employed a mouse model of uterine surgical scarring and identified a stiffness gradient from healthy to scarred uterine tissue. While durotaxis has been widely observed in various cell types, whether mammalian embryos exhibit durotaxis has remained an open question. Using custom-designed polyacrylamide hydrogels with tunable stiffness gradients, we discovered that peri-implantation stage mouse embryos and human-derived trophoblast cell spheroids consistently exhibit durotaxis. Through integrative mechanical modeling, we uncovered that the embryonic durotaxis is initiated by asymmetric adhesion forces and driven by cell blebbing induced by an internal Marangoni flow. The durotaxis of embryos display complex migration modes, including translation, swing, and rolling and uniquely characterized by periodic migration patterns synchronized with embryo cavity oscillations. Finally, inhibiting cell blebbing significantly reduces the risk of CSP in our mouse model. These findings pioneer the concept of embryonic durotaxis and establish a mechanical framework for understanding CSP development, which opens new therapeutic avenues for intervention and management of CSP.

INTRODUCTION

Cesarean scar pregnancy (CSP) is an increasingly recognized complication linked to the rising global rate of cesarean sections (CS) [1,2]. Evidence suggests that women with a history of CS are more likely to experience embryo implantation in the cesarean scar [3] and the risk increases with the number of CS[2]. In other words, compared to patients without a history of CS, patients with CS tended to implant their embryo in the cesarean scar, that is, CSP. As pregnancy progresses in CSP cases, the risk of severe complications escalates significantly, including uterine rupture, massive hemorrhage, and life-threatening maternal outcomes [4,5]. Given the substantial risks associated with CSP, it has garnered increasing attention from both researchers and clinicians, highlighting the urgent need for improved diagnostic and therapeutic strategies to mitigate these adverse outcomes [6,7]. However, the pathogenesis of CSP remains incompletely elucidated.

Embryo implantation, a precisely orchestrated biological process, unfolds through three sequential stages: apposition, adhesion, and invasion [8,9]. The initial stages of apposition and adhesion play a pivotal role in determining the implantation site, during which the embryo undergoes a dynamic rolling motion along the uterine wall to identify an optimal location for implantation [10,11]. Current research on CSP pathogenesis has predominantly focused on the severe progression of the disease, particularly emphasizing the aberrant healing process of uterine incisions [12,13]. Several contributing factors have been proposed, including local hypoxia, altered vascular patterns, and immune modulation at the scar site [14]. However, there lacks research on the mechanism why embryos are more likely to implant on cesarean scars. This could be the key to preventing the CSP from occurring.

Emerging evidences have revealed that scar biomechanics drives disease progression by altering tissue mechanics which exacerbate pathological processes such as fibrosis, impaired wound healing, and tumor microenvironment remodeling [15-17]. Through sonoelastographic analysis, Elvira di Pasquo *et al*. demonstrated that uterine scars exhibit substantially increased stiffness compared to adjacent myometrium, with a strain ratio of 1.8 ± 0.7 [18]. Despite these findings, the influence of mechanical properties on CSP pathogenesis remains relatively underexplored in current scientific literature.

Recent studies have increasingly demonstrated that numerous cell types exhibit durotaxis, a mechanosensitive phenomenon in which cells migrate individually or collectively toward regions of higher substrate stiffness [19-25]. Our previous research revealed that JAR cells, a human trophoblast cell

line, also display durotactic behavior, suggesting that mechanical cues may play a guiding role in trophoblast migration during embryo implantation [26]. Considering that cesarean scar tissue typically exhibits significantly higher stiffness compared to the adjacent healthy uterine tissue [18,27], it is plausible that embryonic durotaxis could contribute to the pathogenesis of CSP. However, whether mammalian embryos exhibit durotaxis and how this active mechanotactic behavior influences CSP development remain poorly understood and warrant further investigation.

In this study, we quantified the mechanical alterations in cesarean scar tissue using a mouse model of uterine surgical scarring, revealing a stiffness gradient that progressively increases from healthy to scarred regions. To mimic the mechanical environment of cesarean scar tissue, we employed tunable polyacrylamide hydrogels and discovered that peri-implantation stage mouse embryos and human-derived trophoblast cell spheroids exhibit durotactic migration. This migration is uniquely characterized by periodic behavior driven by blastocyst cavity oscillation, uncovering a novel link between mechanical cues and embryonic dynamics. Further analysis revealed that embryonic durotaxis within a single period encompasses multiple migration modes, including translational movement, in-plane rotations, and out-of-plane rotations. By integrating experimental approaches with mechanical modeling, we demonstrated that embryo durotaxis is initiated by asymmetric substrate adhesion and largely enhanced by polarized surface fluctuations. Most importantly, using our uterine surgical scarring mouse model, we showed that inhibiting surface fluctuations significantly reduces the risk of CSP, offering a potential therapeutic strategy for preventing this condition.

RESULTS

Mouse embryos display durotactic migration

To investigate the impact of cesarean sections on embryo implantation, we developed a mouse model of uterine surgical scarring, building upon previous research methodologies [28-31] (Fig. 1A). In the murine uterine scar model, histological features comparable to cesarean section-induced myometrial disruption and subsequent scar tissue repair can be observed at the uterine scar site (Supplementary Fig. S1A-C). Quantitative analysis of implantation site distribution revealed a significantly higher percentage of implantation sites located in scarred regions compared to adjacent non-scarred regions (Fig. 1C), Moreover, embryos implanted in scarred regions exhibited significantly poorer pregnancy outcomes, characterized by elevated rates of pregnancy loss and embryonic resorption in mice with metratomy (Supplementary Fig. S1D and E). These results provide evidence for the association between CSP and cesarean sections in murine models.

To elucidate the role of mechanical properties of scarred uterine in CSP pathogenesis, we first employed Atomic Force Microscopy (AFM) to measure tissue stiffness in both scarred and adjacent healthy regions at embryonic day 3.5 (E3.5) (Fig. 1D). Our measurements demonstrated that scarred regions exhibited significantly higher stiffness compared to surrounding non-scarred tissues (Fig. 1E). Furthermore, we observed a distinct stiffness gradient, characterized by an increasing Young's modulus from non-scarred to scarred regions (Fig. 1F). These findings provide compelling evidence for a correlation between the heightened likelihood of implantation in scarred regions and the presence of a stiffness gradient within the scarred uterine tissues.

To investigate how embryos respond to the stiffness gradient of uterine scar tissue, we cultured mouse embryos at the peri-implantation stage (E4.5) on a polyacrylamide hydrogel substrate system featuring a controlled stiffness gradient [26], simulating the embryo implantation process (Fig. 1G). Time-lapse imaging revealed that embryos exhibited substantial durotactic migration, preferentially moving from softer regions toward stiffer regions on gradient substrates. In contrast, embryos cultured on hydrogels with uniform stiffness (hereafter referred to as uniform substrates) exhibited no such directional migration (Fig. 1H-J). We further quantified durotaxis-related parameters, including Forward Migration Index (FMI), persistence, and velocity [28,32]. Comparative analysis of these parameters between embryos cultured on gradient substrates and uniform substrates demonstrated

significantly enhanced durotaxis on gradient substrates (Fig. 1K-M). Additionally, when comparing these parameters across different stiffness zones (soft, intermediate, and stiff), we observed the most pronounced durotaxis in intermediate regions (Supplementary Fig. S2). These findings demonstrate that mouse embryos exhibit durotaxis on gradient stiffness substrates, mimicking the mechanical properties of uterine surgical scars.

A similar durotactic response was also observed in multicellular spheroids composed of human trophoblast cells (JAR, Supplementary Fig. S3A-F), consistent with our previous findings in single JAR cells [26]. However, comparative analysis of durotactic-related parameters between JAR spheroids and mouse embryos cultured on hydrogels with identical stiffness gradients revealed that embryos exhibited significantly more pronounced durotaxis (Supplementary Fig. S3G-I). Collectively, these results provide critical insights into the role of tissue stiffness gradients in guiding embryo implantation dynamics.

Durotaxis of mouse embryos is initiated through the establishment of an asymmetric trophectoderm-substrate adhesion pattern

Extensive studies have demonstrated the critical role of cell-substrate interactions in the durotaxis of both single cells and cell collectives [33-35]. In our experiments, we analyzed embryo-substrate interactions by monitoring trophectoderm cell membrane at the embryo-substrate interface in $mTmG^{+/-}$ embryos. Time-lapse imaging revealed that during the initial interaction between embryos and substrates, membrane signals at the trophectoderm-substrate interface were predominantly detected on the stiffer side of the substrate, indicating that an asymmetric interaction pattern that aligned with the stiffness gradient of substrates (Fig. 2A-C). As adhesion progressed, the membrane signal intensity on the stiff side showed a significantly greater increase compared to the soft side, with this disparity becoming progressively more pronounced over time (Fig. 2D and E). This asymmetric adhesion pattern was consistently observed during JAR spheroid-substrate interactions, where the spatial distribution of Vinculin-GFP and Lifeact-mCherry signals at the interface exhibited similar asymmetry (Supplementary Fig. S4). These findings collectively demonstrate that the initiation of embryonic adhesion to substrates with stiffness gradients establishes a distinct asymmetric trophectoderm-substrate adhesion pattern.

To determine whether asymmetric trophectoderm-substrate adhesion is essential for the durotactic migration of mouse embryos, we disrupted trophectoderm-substrate adhesion using integrin inhibitor—RGD peptides [36]. RGD treatment significantly reduced the spatial asymmetry of focal adhesion (FA) distribution at the trophectoderm-substrate interface (Fig. 3F). Quantitative analysis of durotaxis-related parameters demonstrated a significant decrease in the durotactic response of RGD-treated embryos compared to DMSO-treated controls (Fig. 3G and H). Consistent with these findings, RGD treatment similarly impaired durotactic migration in JAR spheroids (Fig. 3I and J). Given that substrate adhesion represents the initial step in embryo-substrate interactions, these results establish that the formation of an asymmetric trophectoderm-substrate adhesion pattern is prerequisite for initiating embryonic durotactic migration.

Polarized trophectoderm cell blebbing is essential for embryonic durotaxis

During the analysis of embryo surface contours, we found progressive spatiotemporal surface fluctuations of trophectoderm over time during embryo migration on stiffness gradient substrates which was not observed on substrate with uniform stiffness (Fig. 4A). Strikingly, surface fluctuations were significantly more pronounced on the stiff side compared to the soft side, demonstrating the formation of polarized surface fluctuations during embryonic durotaxis (Fig. 3A-E). By quantifying surface curvature, we identified two distinct types of surface fluctuations: large-scale fluctuations associated with cellular blebs and small-scale fluctuations linked to extruded cells (Fig. 3F and G). Consistent results were observed in EYFP-mem^{+} JAR spheroids (Supplementary Fig. S5). These findings provide strong evidence for a direct correlation between the polarity of cellular blebbing and the directionality of embryonic durotaxis.

To further investigate single-cell behaviors within embryos during durotactic migration, we labeled cell nuclei with SPY555. Time-lapse imaging revealed a significantly higher density of trophectoderm cells on the stiff side compared to the soft side, indicating polarized cellular crowding within the embryos (Fig. 4A). Furthermore, trophectoderm cell nuclei on the stiff side exhibited a more flattened morphology than those on the soft side, suggesting polarized nuclear deformation in response to substrate stiffness gradients (Fig. 4G). Recent studies have highlighted the critical role of nuclear deformation in driving cell blebbing, a process mediated by cytosolic phospholipase A2 (cPLA2)

signaling [37]. To investigate the role of nuclear deformation-induced cell blebbing, we treated embryos with AACOCF3, a specific inhibitor of cPLA2 [37,38]. This treatment significantly reduced the extent of trophectoderm cell blebbing and abolished their polarity (Fig. 4H). Quantification of durotaxis-related parameters demonstrated that AACOCF3 treatment significantly decreased the extent of embryonic durotaxis (Fig. 4I). Consistent results were observed in EGFP-NLS$^+$ and EYFP-mem$^+$ JAR spheroids (Supplementary Fig. S5). Collectively, these findings demonstrate that polarized trophectoderm cell blebbing, driven by nuclear deformation, is essential for driving embryonic durotaxis.

A Marangoni-like flow mechanism drives multi-modal durotaxis of embryos

To investigate the mechanisms underlying durotactic migration in embryos, we employed live-cell dye staining to visualize cell nuclei, enabling precise tracking of migratory patterns. Intriguingly, unlide single-cell durotaxis on 2D substrates—which exhibits only translation movement (migration without rotations)—mouse embryos displayed multiple migration modes, including translation, rolling (out-of-plane rotation with an axis parallel to the substrate), and swing (in-plane rotation with an axis perpendicular to the substrate) (Fig. 5A). We assessed migration efficiency by measuring FMI, persistence, and velocity during embryo durotaxis. Notably, translation and swing modes exhibited higher FMI, persistence, and velocity compared to rolling (Fig. 5B and C). Further analysis revealed that in-plane rotation mode (swing) exhibited the highest velocity than translation and rolling modes of embryo durotaxis (Fig. 5D). These findings demonstrate that the unique combination of migration modes enhances durotaxis of mouse embryos.

To elucidate how blebbing forces generate these migration modes, we developed a mechanical model based on experimental observations (Fig. 5E). In translation mode, trophectoderm cell blebbing exists near the bottom of embryos and the resultant blebbing force F and substrate drag force f oppose each other along the same embryo axis. In contrast, when F and f are misaligned, they generate torque T, inducing either rolling (out-of-plane rotation) or swing (in-plane rotation). Our model explains why the in-plane rotation (swing) is more efficient than other modes (Fig. 5D). For translation, the blebbing force F must exceed the maximum drag ($F \geq f_m$, force f_m from the substrate adhesion). The drag force f consists a substrate friction and a fluid drag force, which is estimated to be on the order of magnitude of ~100 pN (see supplemental materials for details). Thus, to generate a translational motion the

resultant force F from cell blebbing should be larger than 100 pN. While for swing motion, the torque balance requires $Fs = T = 8\pi\mu R^3\omega$, where s is the separation between the parallel forces F and f, μ is fluid viscosity, R is embryo raidus, and ω is angular velocity. The driven force for a swing motion is estimated to approximately $F \sim 0.2$ pN, based on typical values of torque $T \sim 10^{-18}$ N.m and separation s ~ 10 μm. Obviously, the force needed for swing motion is much smaller than that for translational force, explaining our observation (Fig. 5D) that swing motion manifests higher velocity than translational motion. However, rolling is quite different due to strong adhesion to the substrate. Distinct from the swing mode in which only torque balance should be fulfilled and no detachment of the adhesion pattern (as rotation axis) is required, in rolling mode, the detachment of the adhesion means that force and torque conditions (i.e., $F \geq f_m$ and $Fs = T = 8\pi\mu R^3\omega$) must be fulfilled simultaneously. Thus, rolling mode is not an efficient way for embryo to migrate.

We further explored the mechanism of polarized surface fluctuations in embryo durotaxis. Particle Image Velocimetry (PIV) revealed directional cell flows towards the stiff side of embryos which were strongly aligned with surface fluctuations and suppressed by AACOCF3 treatment (Fig. 5F and G). UV laser ablation experiments demonstrated that the stiff side of embryo surface exhibited higher recoil velocity on than the soft side, which suggests surface tension gradients in embryos (Fig. 5H-J). These findings suggest a Marangoni-like flow mechanism—driven by surface tension gradients—the stiff side of the embryo exhibits higher tension, propelling internal cells toward stiff side and increasing local cell density which further causing cell blebbing. Collectively, our findings propose a Marangoni-like flow mechanism, linking substrate stiffness gradients, internal cell movement, and cell blebbing (Fig. 5K). The 3D interplay of blebbing forces and substrate adhesion yields three migration modes, influenced by embryo surface tension, fluidity, cell deformability, and surface fluctuations.

Inhibiting trophectoderm cell blebbing prevents cesarean scar pregnancy in mouse models

Blastocysts are known to exhibit cavity oscillations, characterized by periodic expansion and contraction of the blastocyst cavity [39,40]. Intriguingly, our time-lapse imaging revealed that while JAR spheroids exhibited transient and shorter durotactic migration, embryos displayed periodic and prolonged durotaxis (Fig. 6A). We found that the migration period of mouse embryos closely synchronized with the cycle of these cavity oscillations (Fig. 6B and C). Within a single period,

embryos demonstrated pronounced and continuous migration during the expansion phase of the blastocyst cavity, whereas durotactic migration was disrupted during the contraction phase (Fig. 6B and D). These findings underscore a unique and intricate mode of durotactic migration in mouse embryos, driven by the interplay between substrate-derived mechanical cues and intrinsic embryonic cavity dynamics.

To assess the role of cavity oscillations in embryo durotaxis, we employed aphidicolin to inhibit trophoblast cell division a process essential for diving cavity oscillations [39]. Compared to control embryos, aphidicolin-treated embryos exhibited significantly reduced frequency of both cavity oscillations and durotaxis (Fig. 6E). Moreover, the extent of durotactic migration was strikingly reduced by aphidicolin treatment (Fig. 6F-H). Quantitative analysis revealed that key durotaxis-related parameters—FMI, persistence, and velocity—were all significantly reduced by aphidicolin treatment (Fig. 6I-K). Collectively, these results demonstrate that the cyclic contraction and expansion of the embryo cavity further extend the cell blebbing-driven durotaxis by providing the periodicity of embryo response to substrate stiffness gradient.

Finally, in order to assess the function of embryo durotaxis in the pathogenesis of cesarean scar pregnancy, we investigated whether inhibiting surface fluctuations of embryos would prevent cesarean scar pregnancy by AACOCF3 perfusion treatment in pregnant mice of our established uterine surgical scarring model (Fig. 6L). It was observed that the treatment of AACOCF3 significantly reduced the r number of implantation sites in scarred regions compared to adjacent non-scarred regions, while did not affect the implantation site distribution on the healthy side of uterine (Fig. 6M-O). These findings highlight the contribution of uterine mechanical environment in the implantation site determination and suggest that inhibiting embryo durotaxis could potentially reduce the risk of CSP.

DISCUSSION

Cesarean scar pregnancy, a critical and increasingly recognized obstetric complication, remains poorly understood in terms of its precise pathogenesis, particularly the mechanisms underlying implantation site selection in scarred regions [41-44]. To address this question, we first established a mouse model with uterine scars and identified an increased stiffness gradient from non-scarred to scarred regions in uterine tissue. Using tunable PA hydrogels to mimic changes in the uterus physical microenvironment, we investigated the effect of substrate stiffness gradient on embryo migration. Our study revealed that mouse embryos and human-derived trophoblast cell spheroids exhibited directional migration, known as durotaxis, along the stiffness gradient. During this process, trophectoderm cells at the embryo-substrate interface first sensed the stiffness gradient and established an asymmetric adhesion pattern between the trophectoderm and the substrate. Further investigation demonstrated that the polarized trophectoderm cell blebbing, induced by internal tissue flows within the embryo toward stiffer regions, provided the driving force for embryonic durotaxis through three distinct modes: translational motion, swing, and rolling. Additionally, the periodic contraction and expansion of embryonic cavity introduced a cyclical component to this positive feedback process, further prolonging embryo migration. Finally, using our uterine scar mouse model, we successfully reduced the percentage of implantation site localized in scarred regions by pretreatment with a cell blebbing inhibitor (AACOCF3). Collectively, these findings demonstrate that the biomechanical properties of uterine tissue play a critical role in regulating embryo migration and selection of implantation sites, contributing to the occurrence of CSP.

While this study provides insights into the role of stiffness gradients in embryo migration and implantation, certain limitations should be acknowledged [45]. First, our *in vitro* model utilized mouse embryos, human-derived trophoblast cell spheroids, and stiffness-tunable hydrogels, which do not fully capture the complexity of the uterine environment. Future studies could enhance the model by incorporating endometrial epithelial cells into the hydrogel system, enabling a more accurate simulation of the interactions between trophectoderm cells and the uterine lining. This approach would offer a more comprehensive understanding of the implantation process. Additionally, although mouse embryos were employed in this study, the implantation process in humans differs, particularly in later stages such as trophoblast differentiation and uterine remodeling [46-48]. To address this limitation, the

development of *in vitro* models using human embryos or human-derived tissues could bridge this gap and provide deeper insights into the pathogenesis of CSP. Such advancements would not only improve the translational relevance of the findings but also pave the way for more targeted therapeutic strategies for implantation-related disorders.

In summary, this work demonstrates that embryo migration and adhesion are mechanically sensitive processes, underscoring the importance of extracellular tissue engineering strategies to advance our understanding and treatment of implantation-related disorders. These mechanobiological insights hold significant potential for improving technologies aimed at enhancing the success rates of in vitro fertilization (IVF). Moreover, elucidating these mechanically mediated mechanisms may uncover new regulatory pathways governing embryonic adhesion, paving the way for innovative therapeutic approaches to address pregnancy-related complications. By integrating biomechanical principles with reproductive medicine, this work opens new avenues for both fundamental research and clinical applications in the field of obstetrics and fertility.

REFERENCES

1 Clark, S. L., Koonings, P. P. & Phelan, J. P. Placenta previa/accreta and prior cesarean section. *Obstet Gynecol* **66**, 89-92 (1985).

2 To, W. W. & Leung, W. C. Placenta previa and previous cesarean section. *Int J Gynaecol Obstet* **51**, 25-31, doi:10.1016/0020-7292(95)80004-v (1995).

3 Jauniaux, E. *et al.* FIGO consensus guidelines on placenta accreta spectrum disorders: Epidemiology. *Int J Gynaecol Obstet* **140**, 265-273, doi:10.1002/ijgo.12407 (2018).

4 Birch Petersen, K., Hoffmann, E., Rifbjerg Larsen, C. & Svarre Nielsen, H. Cesarean scar pregnancy: a systematic review of treatment studies. *Fertil Steril* **105**, 958-967, doi:10.1016/j.fertnstert.2015.12.130 (2016).

5 Gonzalez, N. & Tulandi, T. Cesarean Scar Pregnancy: A Systematic Review. *J Minim Invasive Gynecol* **24**, 731-738, doi:10.1016/j.jmig.2017.02.020 (2017).

6 Krüger-Genge, A., Blocki, A., Franke, R. P. & Jung, F. Vascular Endothelial Cell Biology: An Update. *Int J Mol Sci* **20**, doi:10.3390/ijms20184411 (2019).

7 Mao, X. *et al.* Crosstalk between cancer-associated fibroblasts and immune cells in the tumor microenvironment: new findings and future perspectives. *Mol Cancer* **20**, 131, doi:10.1186/s12943-021-01428-1 (2021).

8 Aplin, J. D. & Ruane, P. T. Embryo-epithelium interactions during implantation at a glance. *J Cell Sci* **130**, 15-22, doi:10.1242/jcs.175943 (2017).

9 Singh, H. & Aplin, J. D. Adhesion molecules in endometrial epithelium: tissue integrity and embryo implantation. *J Anat* **215**, 3-13, doi:10.1111/j.1469-7580.2008.01034.x (2009).

10 Wang, H. & Dey, S. K. Roadmap to embryo implantation: clues from mouse models. *Nat Rev Genet* **7**, 185-199, doi:10.1038/nrg1808 (2006).

11 Paria, B. C., Huet-Hudson, Y. M. & Dey, S. K. Blastocyst's state of activity determines the "window" of implantation in the receptive mouse uterus. *Proc Natl Acad Sci U S A* **90**, 10159-10162, doi:10.1073/pnas.90.21.10159 (1993).

12 Timor-Tritsch, I. E. & Monteagudo, A. Unforeseen consequences of the increasing rate of cesarean deliveries: early placenta accreta and cesarean scar pregnancy. A review. *Am J Obstet Gynecol* **207**, 14-29, doi:10.1016/j.ajog.2012.03.007 (2012).

13 Pędraszewski, P., Wlaźlak, E., Panek, W. & Surkont, G. Cesarean scar pregnancy – a new challenge for obstetricians. *Journal of Ultrasonography* **18**, 56 - 62 (2018).

14 Hameed, M. S. S., Wright, A. & Chern, B. S. M. Cesarean Scar Pregnancy: Current Understanding and Treatment Including Role of Minimally Invasive Surgical Techniques. *Gynecol Minim Invasive Ther* **12**, 64-71, doi:10.4103/gmit.gmit_116_22 (2023).

15 Rybinski, B., Franco-Barraza, J. & Cukierman, E. The wound healing, chronic fibrosis, and cancer progression triad. *Physiol Genomics* **46**, 223-244, doi:10.1152/physiolgenomics.00158.2013 (2014).

16 Timor-Tritsch, I. E., Monteagudo, A., Calì, G., D'Antonio, F. & Kaelin Agten, A. Cesarean Scar Pregnancy: Diagnosis and Pathogenesis. *Obstet Gynecol Clin North Am* **46**, 797-811, doi:10.1016/j.ogc.2019.07.009 (2019).

17 Cox, T. R. & Erler, J. T. Remodeling and homeostasis of the extracellular matrix: implications for fibrotic diseases and cancer. *Dis Model Mech* **4**, 165-178, doi:10.1242/dmm.004077 (2011).

18 di Pasquo, E. *et al.* Evaluation of the uterine scar stiffness in women with previous Cesarean section by ultrasound elastography: A cohort study. *Clin Imaging* **64**, 53-56, doi:10.1016/j.clinimag.2020.03.006 (2020).

19 Lo, C. M., Wang, H. B., Dembo, M. & Wang, Y. L. Cell movement is guided by the rigidity of the substrate. *Biophys J* **79**, 144-152, doi:10.1016/s0006-3495(00)76279-5 (2000).

20 DuChez, B. J., Doyle, A. D., Dimitriadis, E. K. & Yamada, K. M. Durotaxis by Human Cancer Cells. *Biophys J*

116, 670-683, doi:10.1016/j.bpj.2019.01.009 (2019).

21 Vincent, L. G., Choi, Y. S., Alonso-Latorre, B., del Álamo, J. C. & Engler, A. J. Mesenchymal stem cell durotaxis depends on substrate stiffness gradient strength. *Biotechnol J* **8**, 472-484, doi:10.1002/biot.201200205 (2013).

22 Bennett, M. R., Sinha, S. & Owens, G. K. Vascular Smooth Muscle Cells in Atherosclerosis. *Circ Res* **118**, 692-702, doi:10.1161/circresaha.115.306361 (2016).

23 Sunyer, R. *et al.* Collective cell durotaxis emerges from long-range intercellular force transmission. *Science* **353**, 1157-1161, doi:10.1126/science.aaf7119 (2016).

24 Martinez, J. S., Schlenoff, J. B. & Keller, T. C., 3rd. Collective epithelial cell sheet adhesion and migration on polyelectrolyte multilayers with uniform and gradients of compliance. *Exp Cell Res* **346**, 17-29, doi:10.1016/j.yexcr.2016.06.002 (2016).

25 Sunyer, R. & Trepat, X. Durotaxis. *Curr Biol* **30**, R383-r387, doi:10.1016/j.cub.2020.03.051 (2020).

26 Cao, J. *et al.* Stiff Extracellular Matrix Promotes Invasive Behaviors of Trophoblast Cells. *Bioengineering (Basel)* **10**, doi:10.3390/bioengineering10030384 (2023).

27 González-Muñoz, A., Pruimboom, L. & Navarro-Ledesma, S. The Relationship Between the Elastic Properties and Pain Pressure Threshold in Cesarean Scar Tissue-An Observational Study. *Healthcare (Basel)* **12**, doi:10.3390/healthcare12212166 (2024).

28 Zhang, E. T. Mouse Surgical Model of Mechanical Uterine Injury and Subsequent Embryo Defects. *Curr Protoc* **4**, e1044, doi:10.1002/cpz1.1044 (2024).

29 Li, Z. *et al.* Uterine Scarring Leads to Adverse Pregnant Consequences by Impairing the Endometrium Response to Steroids. *Endocrinology* **161**, doi:10.1210/endocr/bqaa174 (2020).

30 Debras, E., Capmas, P., Maudot, C. & Chavatte-Palmer, P. Uterine wound healing after caesarean section: A systematic review. *Eur J Obstet Gynecol Reprod Biol* **296**, 83-90, doi:10.1016/j.ejogrb.2024.02.045 (2024).

31 Buhimschi, C. S., Zhao, G., Sora, N., Madri, J. A. & Buhimschi, I. A. Myometrial wound healing post-Cesarean delivery in the MRL/MpJ mouse model of uterine scarring. *Am J Pathol* **177**, 197-207, doi:10.2353/ajpath.2010.091209 (2010).

32 Yang, F. *et al.* Directional Cell Migration Guided by a Strain Gradient. *Small* **20**, e2302404, doi:10.1002/smll.202302404 (2024).

33 Bose, S., Wang, H., Xu, X., Gopinath, A. & Dasbiswas, K. Elastic interactions compete with persistent cell motility to drive durotaxis. *Biophys J* **123**, 3721-3735, doi:10.1016/j.bpj.2024.09.021 (2024).

34 Mathieu, M., Isomursu, A. & Ivaska, J. Positive and negative durotaxis - mechanisms and emerging concepts. *J Cell Sci* **137**, doi:10.1242/jcs.261919 (2024).

35 Espina, J. A., Marchant, C. L. & Barriga, E. H. Durotaxis: the mechanical control of directed cell migration. *Febs j* **289**, 2736-2754, doi:10.1111/febs.15862 (2022).

36 Yamada, Y. *et al.* Structure-Activity Relationships of RGD-Containing Peptides in Integrin αvβ5-Mediated Cell Adhesion. *ACS Omega* **8**, 4687-4693, doi:10.1021/acsomega.2c06540 (2023).

37 Lomakin, A. J. *et al.* The nucleus acts as a ruler tailoring cell responses to spatial constraints. *Science* **370**, doi:10.1126/science.aba2894 (2020).

38 Linkous, A., Geng, L., Lyshchik, A., Hallahan, D. E. & Yazlovitskaya, E. M. Cytosolic phospholipase A2: targeting cancer through the tumor vasculature. *Clin Cancer Res* **15**, 1635-1644, doi:10.1158/1078-0432.Ccr-08-1905 (2009).

39 Guo, Z. *et al.* Cavity oscillation drives pattern formation in early mammalian embryos. *Cell Rep* **44**, 115342, doi:10.1016/j.celrep.2025.115342 (2025).

40 Alasaadi, D. N. & Mayor, R. Mechanically guided cell fate determination in early development. *Cell Mol Life Sci* **81**, 242, doi:10.1007/s00018-024-05272-6 (2024).

41 Timor-Tritsch, I. E. *et al.* Cesarean scar pregnancy and early placenta accreta share common histology. *Ultrasound Obstet Gynecol* **43**, 383-395, doi:10.1002/uog.13282 (2014).

42 Kaelin Agten, A. *et al.* The clinical outcome of cesarean scar pregnancies implanted "on the scar" versus "in the niche". *Am J Obstet Gynecol* **216**, 510.e511-510.e516, doi:10.1016/j.ajog.2017.01.019 (2017).

43 Silva, B., Viana Pinto, P. & Costa, M. A. Cesarean Scar Pregnancy: A systematic review on expectant management. *Eur J Obstet Gynecol Reprod Biol* **288**, 36-43, doi:10.1016/j.ejogrb.2023.06.030 (2023).

44 Liu, D., Yang, M. & Wu, Q. Application of ultrasonography in the diagnosis and treatment of cesarean scar pregnancy. *Clin Chim Acta* **486**, 291-297, doi:10.1016/j.cca.2018.08.012 (2018).

45 Fujiwara, H. *et al.* Factors Regulating Human Extravillous Trophoblast Invasion: Chemokine-peptidase and CD9-integrin Systems. *Curr Pharm Biotechnol* **19**, 764-770, doi:10.2174/1389201019666181029164906 (2018).

46 Soncin, F., Natale, D. & Parast, M. M. Signaling pathways in mouse and human trophoblast differentiation: a comparative review. *Cell Mol Life Sci* **72**, 1291-1302, doi:10.1007/s00018-014-1794-x (2015).

47 Red-Horse, K. *et al.* Trophoblast differentiation during embryo implantation and formation of the maternal-fetal interface. *J Clin Invest* **114**, 744-754, doi:10.1172/jci22991 (2004).

48 Silva, J. F. & Serakides, R. Intrauterine trophoblast migration: A comparative view of humans and rodents. *Cell Adh Migr* **10**, 88-110, doi:10.1080/19336918.2015.1120397 (2016).

49 Cai, P. *et al.* Bio-Inspired Mechanotactic Hybrids for Orchestrating Traction-Mediated Epithelial Migration. *Adv Mater* **28**, 3102-3110, doi:10.1002/adma.201505300 (2016).

50 Guan, D. *et al.* Direct Measurement of Optical Force Induced by Near-Field Plasmonic Cavity Using Dynamic Mode AFM. *Sci Rep* **5**, 16216, doi:10.1038/srep16216 (2015).

51 Guan, D. *et al.* Unified description of compressive modulus revealing multiscale mechanics of living cells. *Physical Review Research* **3**, 043166, doi:10.1103/PhysRevResearch.3.043166 (2021).

52 Hertz, H. The contact of elastic solids. *J Reine Angew, Math* **92**, 156-171 (1881).

MATERIALS AND METHODS

Fabrication of Polyacrylamide Hydrogels with Stiffness Gradients

Polyacrylamide (PA) hydrogels with stiffness gradients were fabricated to mimic the mechanical properties of uterine tissue. A polymer solution was prepared by mixing 20% (v/v) acrylamide monomer (Bio-Rad) and 0.4% (v/v) N, N'-methylenebisacrylamide cross-linker (Bio-Rad) in 1× Dulbecco's phosphate-buffered saline (PBS, Life Technologies, Gaithersburg, MD, USA) without Mg^{2+} and Ca^{2+}. The solution was degassed for 5 minutes, after which 4 μL of 10% (w/v) ammonium persulfate (APS, Sigma-Aldrich) was added and mixed for 0.5 seconds. Subsequently, 1.2 μL of N, N, N', N'-tetramethylethylenediamine (TEMED, Bio-Rad) was rapidly added and mixed for 1 second. A 120 μL aliquot of the solution was transferred into a glass mold, and a functionalized glass coverslip was placed over the solution at an angle to prevent air bubbles. Polymerization was allowed to proceed for 30 minutes at room temperature, after which the coverslip was removed. The gels were rinsed and stored in 1× PBS without Mg^{2+} and Ca^{2+} for later use.

To enable cell adhesion, the PA gel surface was functionalized using Sulfosuccinimidyl 6-(4'-azido-2'-nitrophenylamino) hexanoate (sulfo-SANPAH, Thermo Fisher Scientific, Waltham, MA, USA). The gel was exposed to sulfo-SANPAH for 15 minutes under 365 nm UV light (twice) and then coated with collagen I (100 μg/mL) overnight at 4°C. Prior to cell seeding, the PA gels were washed three times with PBS. These PA hydrogels exhibited a thickness gradient and an apparent stiffness gradient, as previously described [49]. The thickness of the PA gel was measured by staining the gel with Coomassie brilliant blue G-250 for 10 minutes. Z-stack images were acquired using a confocal microscope (Leica TCS SP8 X, Germany) and reconstructed to determine the gel's thickness.

The apparent Young's modulus of the PA gel was assessed using an atomic force microscope (AFM, MFP-3D, Asylum Research Inc., Santa Barbara, CA, USA) equipped with a colloidal probe cantilever. A non-tip cantilever (NSC36, MikroMasch, Watsonville, CA, USA) with a spring constant of 2 N/m was used. The colloidal probe, consisting of a glass sphere (d = 26.3 μm) adhered to the cantilever's front end, was prepared as described previously [50]. To minimize adhesion between the probe and the PA gel, the colloidal probe surface was coated with PLL-g-PEG (SuSoS AG) [51]. AFM measurements were performed in contact mode with indentation depths of 1–8 μm. Force-distance curves were

recorded and analyzed using the Hertz model $F = \frac{4}{3(1-\nu^2)} E R^{0.5} \delta^{1.5}$ to determine the reduced Young's modulus E [52], where F is the force, R is the probe radius, δ is the indentation distance, and $\nu = 0.33$ represents the Poisson ratio. The spring constant of the colloidal probe was calibrated in situ before each measurement using the thermal power spectral density method [50].

The surface topography of the PA gel was examined using scanning electron microscopy (SEM, Quanta 200 FEG). The gels were flash-frozen and lyophilized overnight, followed by sputter-coating with a layer of platinum (Pt) using a turbomolecular pump coater (Q150T, Quorum Technologies, Lewis, UK) to enhance electrical conductivity. Each PA gel was fabricated under consistent conditions across independent experiments, and reproducibility was verified by controlling the size, thickness, and partitioning of the gels.

Embryo Collection and Culture

Preimplantation embryos were collected from female mice (aged 2 to 3 months) to study their behavior in vitro. To induce superovulation, female mice were intraperitoneally injected with 10 international units (IU) of pregnant mare serum gonadotropin (PMSG; Solarbio, P9970). Forty-eight hours later, the mice were injected with 10 IU of human chorionic gonadotropin (hCG; ShuSheng, 11025). Immediately after the hCG injection, the female mice in the superovulation phase were mated with male mice (aged 3 to 4 months). Preimplantation embryos were collected by flushing the uterus or fallopian tubes with KSOM medium (Caisson, IVL04). The collected embryos were then cultured in drops of KSOM under mineral oil (Sigma, M8410) at 37°C in a 5% CO_2 atmosphere. Both the mineral oil and KSOM medium were preheated in the incubation chamber for at least 30 minutes prior to embryo culture to ensure optimal conditions. All embryo manipulations were performed using a stereo microscope (Olympus SZX16).

General Cell Culture

The JAR human choriocarcinoma cell line (TCHu156, ATCC) was maintained in RPMI 1640 medium (Hyclone) at 37°C in a humidified incubator with 5% CO_2. The culture medium was supplemented with 10% (v/v) fetal bovine serum (FBS, SERANA), 100 units/mL penicillin, and 100 units/mL

streptomycin.

JAR Spheroid Formation

For the spheroid formation assay, JAR cells were seeded at a density of 1×10^5 cells/mL in 100 μL per well in an ultra-low attachment 96-well round-bottom plate (Corning, NY, USA). Cells were incubated overnight at 37°C in a 5% CO_2 incubator. During this incubation, JAR cells naturally aggregated to form spheroids with diameters ranging from 50 to 200 μm. The aggregate diameters of the spheroids were measured using CellSens standard software (Olympus, Tokyo, Japan).

Mice

All study involving animals have been reviewed and approved by the Peking University Third Clinical Medical School Ethical Committee of animals (Approval No. A2023001). Eight-week-old CD-1 (CD-1 IGS) mice were purchased from Charles River (Beijing, China). Both male and female mice were purchased and housed in a specific pathogen-free (SPF) animal facility under standard environmental conditions, with constant temperature, humidity and 12h: 12h light cycle. The food and water were available ad libitum.

In this study, pregnancies were created using timed mating. One or two females in estrus were placed with a stud male overnight. Visualization of copulation plug was denoted as embryonic day 0.5 (E0.5)), Successfully mated females were weighted and removed from the stud cage.

Uterine scar mouse model

Virgin mice were used. Mice were anesthetized with isoflurane inhalation anesthesia using a precision vaporizer. 2.5% isoflurane was used for induction, then reduced to 1.5% for maintenance anesthesia throughout the surgery via nosecone. And the oxygen flow was set at 1.5 L/min. A low abdominal incision was made to expose the uterine horns. Chose the right or left uterine horn randomly, and a longitudinal incision of the anti-mesometrial side was made from the cervical side of the uterine horn to the midpoint of the uterine horn. The incision length was half the length of the chosen uterine horn. The incision penetrated through the myometrium and endometrium of the anti-mesometrial side, but did not harm the mesometrial side. The incision was closed with 8-0 absorbable sutures using running locked suture. The end near the midpoint of the uterine horn was marked with 4-0 nonabsorbable

sutures. The uterine was placed back into the abdominal cavity, and the abdominal wall and skin were closed by simple continuous suture with 5-0 absorbable suture respectively.

Following surgery, the mice were permitted to recover for 20 days and mated to fertile male mice. The pregnant mice were humanely killed at different embryonic day.

Particle Image Velocity (PIV) Measurement

Particle Image Velocimetry (PIV) analysis was conducted using a custom algorithm based on MATLAB's PIVlab software package (Matlab2020a, PIVlab2.36). Live cell image sequences of JAR cells were used to analyze the direction and magnitude of cell movement. To mitigate the influence of background movement on the calculated results, the average background velocity was subtracted from the calculated velocity field. For the velocity vector arrows, each pixel length corresponds to 0.05 μm/min.

Statistical Analysis

All statistical analyses were conducted using R software (version 4.1.1). Data are presented as mean ± standard deviation (SD). Each experiment was independently repeated three times (n = 3). Prior to statistical testing, data normality and homogeneity of variances were assessed using the Shapiro–Wilk test and Bartlett's test, respectively. For comparisons between two groups, Student's t-test was applied. A p-value less than 0.05 was considered statistically significant.

ACKNOWLEDGEMENTS

This work was supported by the National Natural Science Foundation of China (No. 12222201, 82273500, 12332019, and under Grant No.12372267), Beijing Nature Science Foundation (No.7232208), Clinical Cohort Construction Program of Peking University Third Hospital (No.2022015) Fundamental Research Funds for the Central Universities (No. ZG140S1971), National Key Research and Development Program of China (No.2023YFF0613604, 2021YFA0719302), and the Strategic Priority Research Program of Chinese Academy of Sciences, Grant No. XDB0620102.

AUTHOR CONTRIBUTIONS

J.D., Y.B.F., Y.W., and X.Z. designed and supervised the experiments and modeling. J.L.C., Y.H.Y., J.W.L. performed the experiments. Y.H.Y., S.P.Y., H.Y.L., and D.S.G. performed the uterine surgical scarring mouse model assays and AFM experiments. Z.X. developed the computational model. All the authors took part in the data analysis. J.L.C., J.D., Y.H.Y., X.Z., and Y.Z. interpreted the data and wrote the paper.

CONFLICT OF INTEREST STATEMENT

The authors declare no competing interests.

Figures

Figure 1

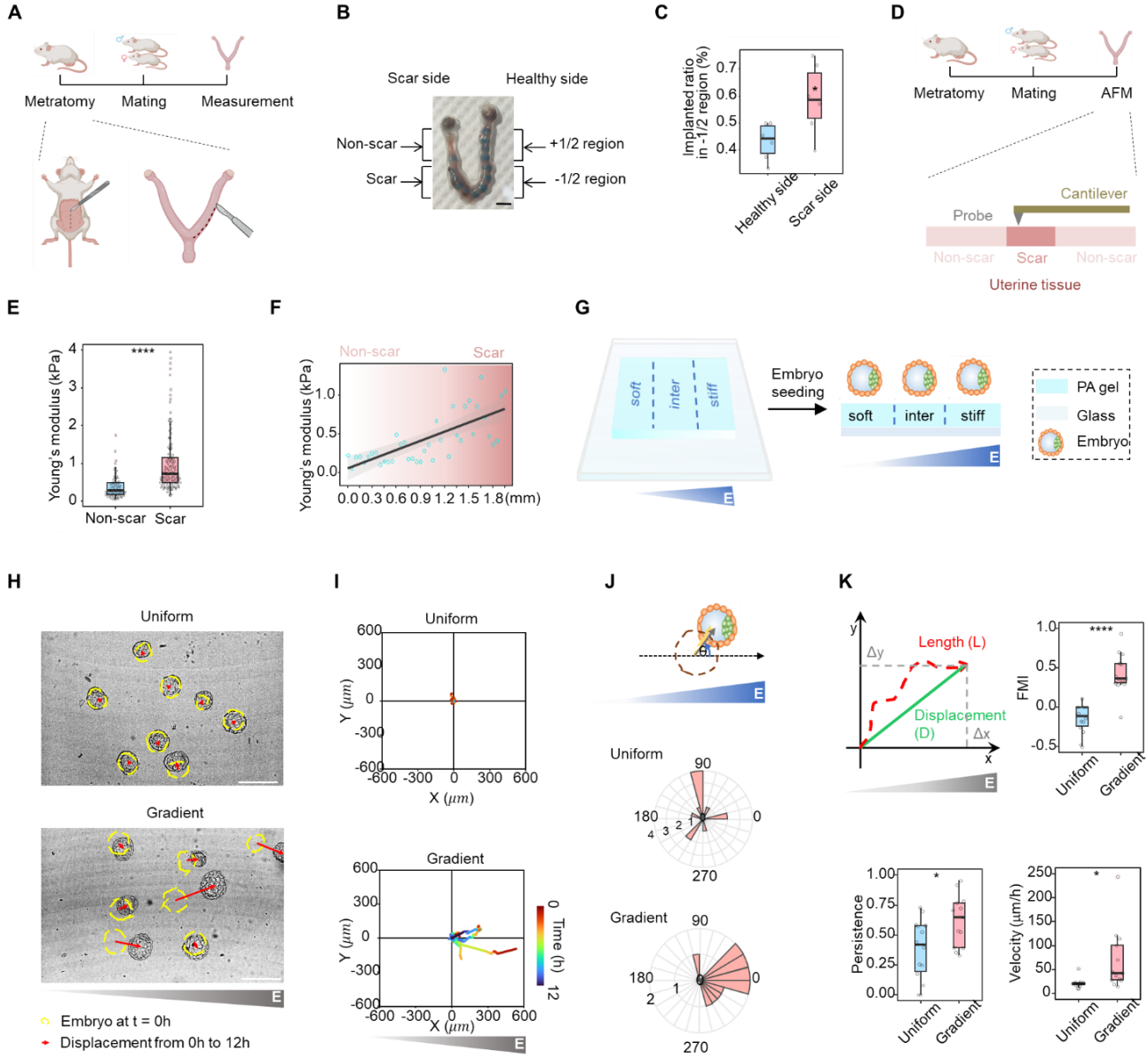

Figure 1. Stiffness gradient in the scarred murine uterine and durotaxis of embryos. (**A**) Schematic illustration of murine uterine scar model. (**B**) The image of implantation sites in murine uterine scar model. Scale bar: 5 mm. (**C**) The statistical analysis of implantation site percentage in -1/2 region at healthy side or scar side of murine uterine scar model, n = 6. (**D**) Schematic illustration of AFM experiments in the scarred murine uterine. (**E**) The statistical analysis of Young's modulus in scarred regions and non-scarred regions in the scarred murine uterine, n = 3. (**F**) The AFM analysis of Young's modulus from non-scarred to scarred regions in the scarred murine uterine. (**G**) Schematic illustration of polyacrylamide hydrogel substrate system featuring a controlled stiffness gradient. (**H**) Representative time-lapse images of embryos on substrates with uniform stiffness or gradient stiffness.

Scale bar: 200 μm. (**I**) Embryo migration plots on gradient substrates over 12 h. (**J**) Rose diagram of embryo migration direction on substrates with uniform stiffness or gradient stiffness, which displays the angular between migration and stiffness gradient and the frequency of each class. (**K**) The statistical analysis of durotaxis-related parameters, including Forward Migration Index (FMI), persistence, and velocity of embryo migration on substrates with uniform stiffness or gradient stiffness, n = 14. All box-and-whisker plots show the medians, maxima, minima, upper quartiles, and lower quartiles. * $p < 0.05$, ** $p < 0.01$, *** $p < 0.001$, **** $p < 0.0001$.

Figure 2

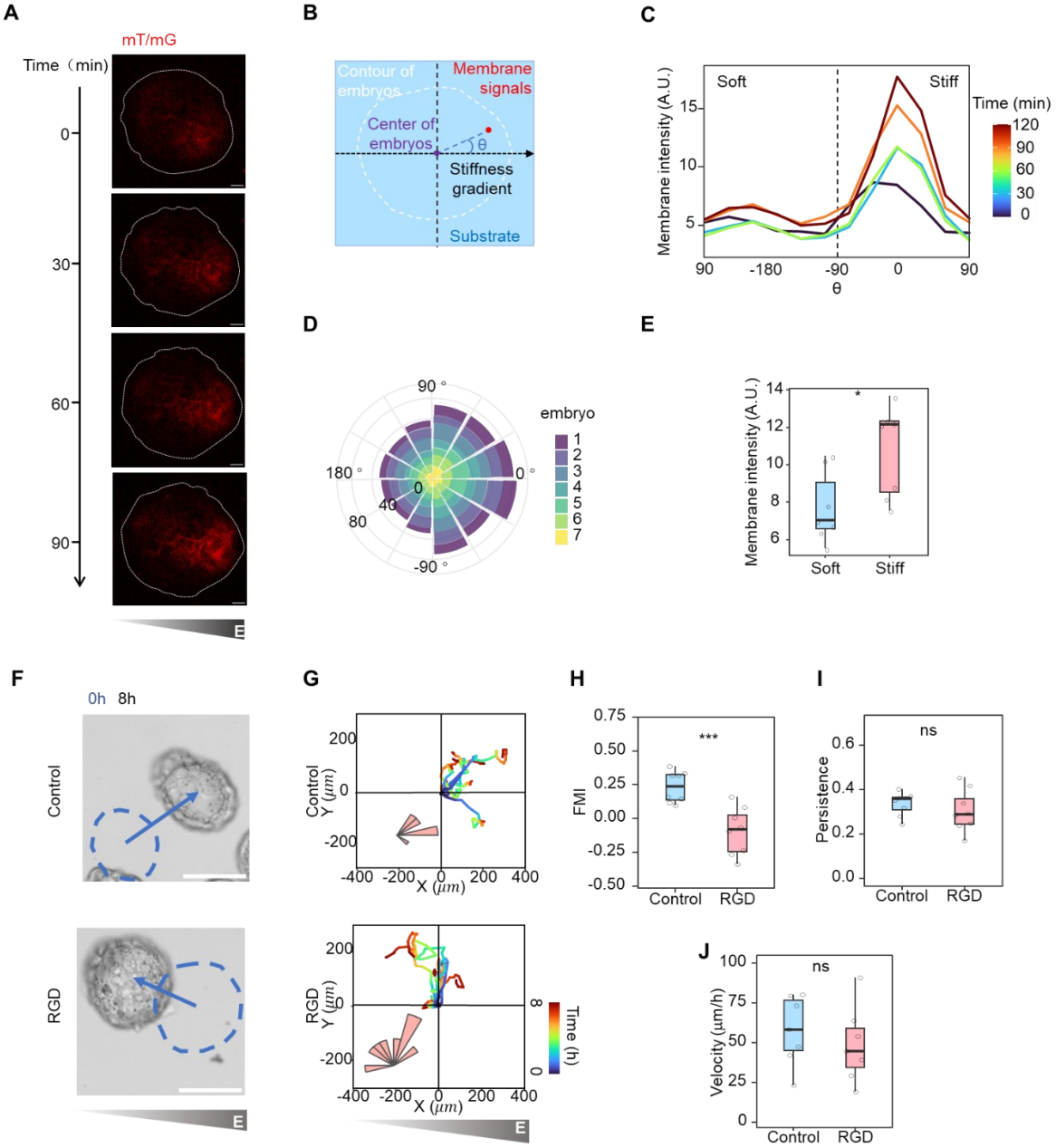

Figure 2. The establishment of an asymmetric trophectoderm-substrate adhesion pattern is required for embryo durotaxis. (**A**) Representative time-lapse fluorescent images of trophectoderm cell membrane at the embryo-substrate interface in mTmG$^{+/-}$ embryos. Scale bar: 20 μm. (**B**) Schematic illustration of angles (θ) between membrane signal related to embryo center and substrate stiffness gradient. (**C**) The membrane intensity at the embryo-substrate interface in mTmG$^{+/-}$ embryos at different angles (θ) during the adhesion of embryos to substrates. (**D**) Rose diagram of membrane

signals at the embryo-substrate interface in $mTmG^{+/-}$ embryos, which displays angles (θ) between membrane signal related to embryo center and substrate stiffness gradient. (**E**) The statistical analysis of membrane intensity at the embryo-substrate interface in soft side (θ: from 90º to -90º) and stiff side (θ: from -90º to 90º) of $mTmG^{+/-}$ embryos, n = 7. (**F**) Representative time-lapse images of embryos on stiffness gradient substrates treated with control or RGD. Scale bar: 100 μm. (**G**) Embryo migration plots on stiffness gradient substrates over 8 h treated with control or RGD. Insets are rose diagram of embryo migration direction, which displays the angular between migration and stiffness gradient and the frequency of each class. (**H-J**) The statistical analysis of durotaxis-related parameters, including Forward Migration Index (FMI), persistence, and velocity of embryo migration on stiffness gradient substrates over 8 h treated with control or RGD, n = 8. All box-and-whisker plots show the medians, maxima, minima, upper quartiles, and lower quartiles. * $p < 0.05$, ** $p < 0.01$, *** $p < 0.001$, **** $p < 0.0001$.

Figure 3

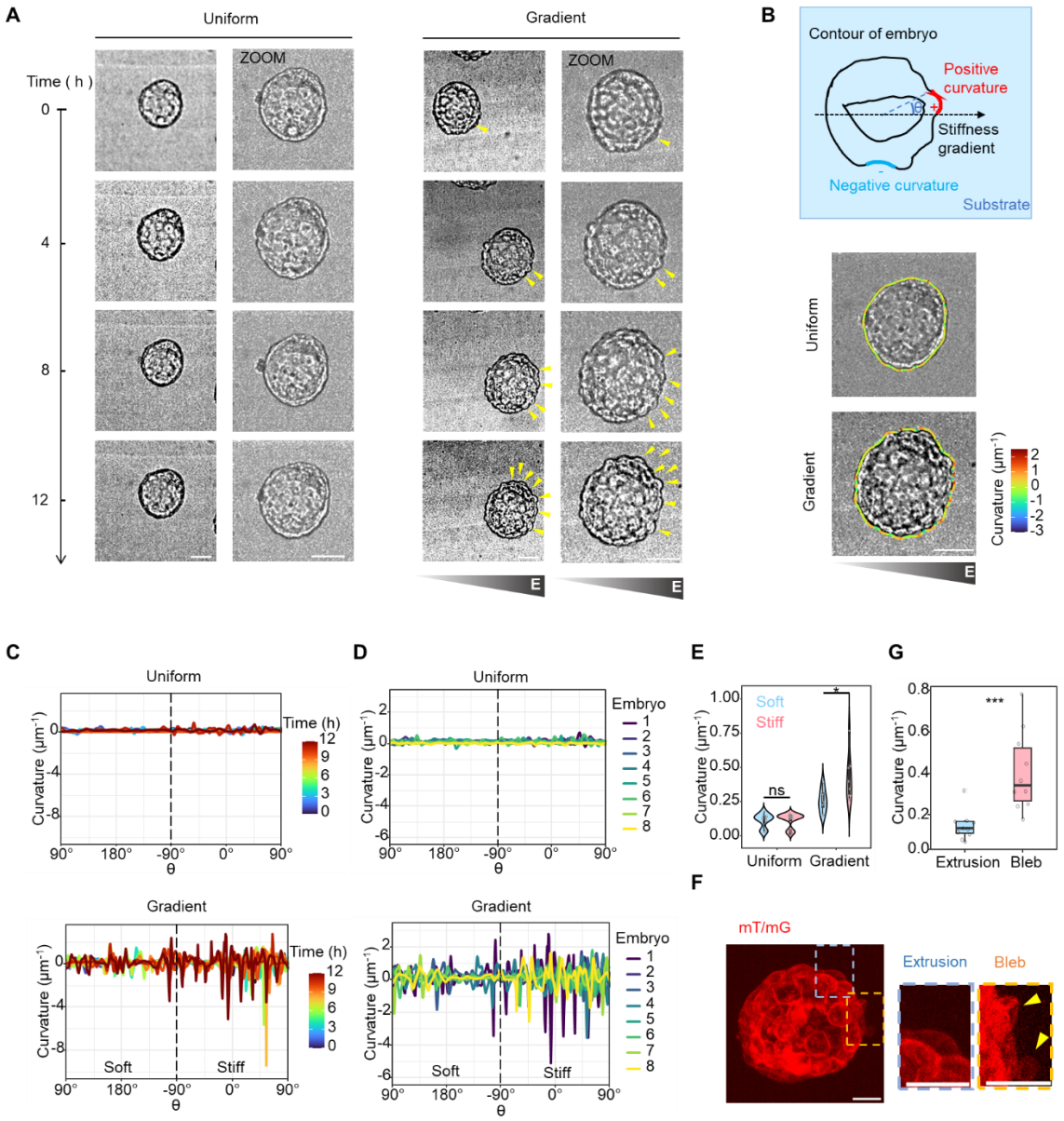

Figure 3. Polarized surface fluctuations during embryo durotaxis on stiffness gradient substrates. (**A**) Representative time-lapse images of embryo surface morphology over time on substrates with uniform stiffness or gradient stiffness. Scale bar: 50 μm. (**B**) The analysis of surface curvature of embryos on substrates with uniform stiffness or gradient stiffness. Scale bar: 50 μm. (**C**) The surface curvature of embryos at different angles (θ) over time on substrates with uniform stiffness or gradient stiffness. (**D**) The surface curvature of embryos at different angles (θ) on substrates with uniform stiffness or gradient stiffness. (**E**) The statistical analysis of surface curvature in soft side (θ: from 90º

to -90º) and stiff side (θ: from -90º to 90º) of embryos on substrates with uniform stiffness or gradient stiffness, n = 8. (**F**) Representative fluorescent images of surface morphology in $mTmG^{+/-}$ embryos. Scale bar: 20 μm. (**G**) The statistical analysis of curvature in two distinct types of cell extrusion and cellular blebs, n = 10. All box-and-whisker plots show the medians, maxima, minima, upper quartiles, and lower quartiles. * $p < 0.05$, ** $p < 0.01$, *** $p < 0.001$, **** $p < 0.0001$.

Figure 4

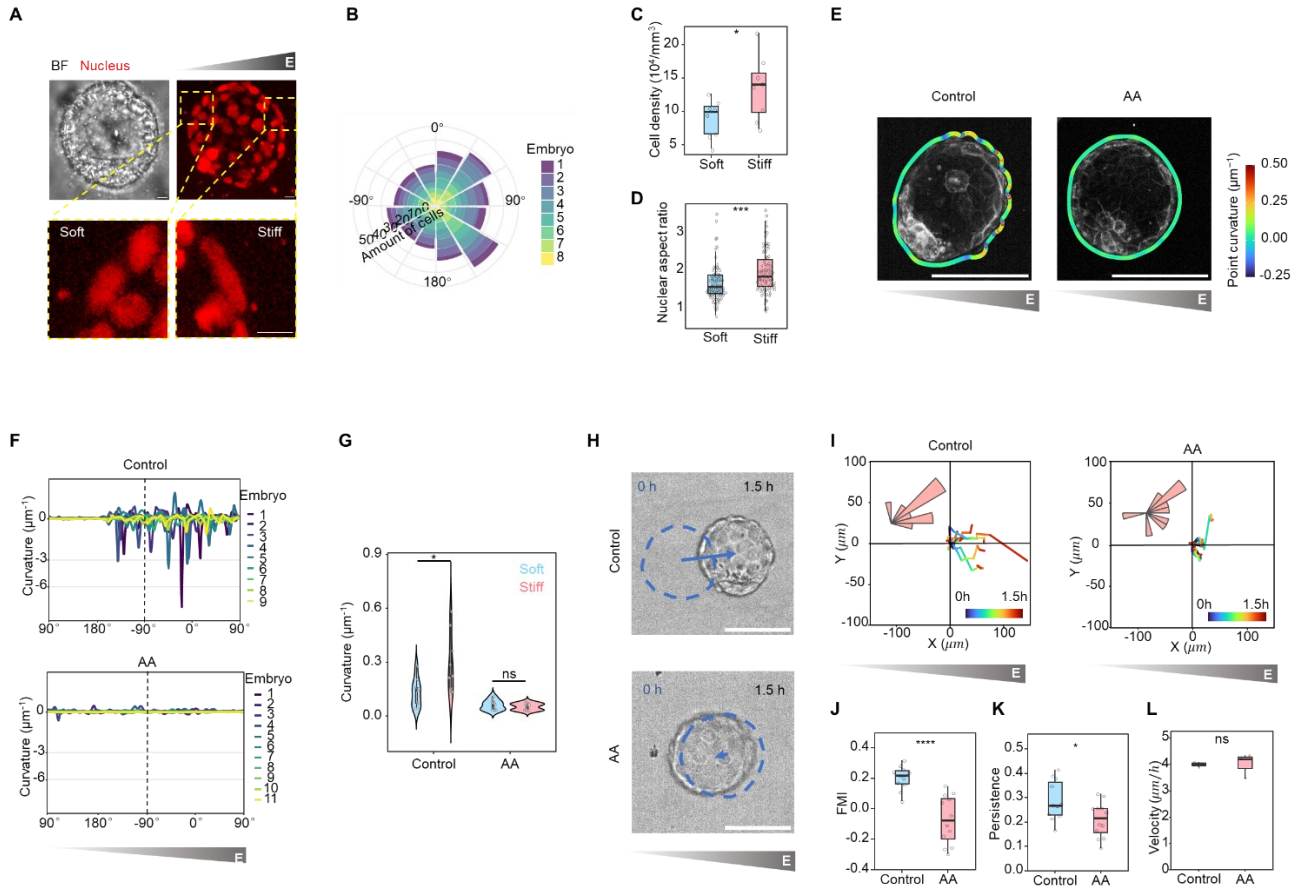

Figure 4. Inhibiting cell blebbing disrupts embryo durotaxis on stiffness gradient substrates. (**A**) Representative fluorescent images of cell nuclei labeled by SPY555 during embryo durotaxis on stiffness gradient substrates. Scale bar: 15 μm. (**B**) The cell density at different angles (θ) on substrates with gradient stiffness. (**C**) The statistical analysis of cell number in soft side (θ: from 90º to -90º) and stiff side (θ: from -90º to 90º) of embryos on stiffness gradient substrates, n = 8. (**D**) The statistical analysis of nuclear aspect ratio in soft side (θ: from 90º to -90º) and stiff side (θ: from -90º to 90º) of embryos on stiffness gradient substrates, n = 8. (**E**) The analysis of embryo surface curvature on stiffness gradient substrates treated with control or AACOCF3. Scale bar: 100 μm. (**F**) The surface curvature of embryos at different angles (θ) on stiffness gradient substrates treated with control or AACOCF3. (**G**) The statistical analysis of surface curvature in soft side (θ: from 90º to -90º) and stiff side (θ: from -90º to 90º) of embryos on stiffness gradient substrates treated with control or AACOCF3, n = 9 (control), 11 (AA). (**H**) Representative time-lapse images of embryos on stiffness gradient substrates treated with control or AACOCF3. Scale bar: 100 μm. (**I**) Embryo migration plots on stiffness gradient substrates over 1.5 h treated with control or AACOCF3. Insets are rose diagram of

embryo migration direction, which displays the angular between migration and stiffness gradient and the frequency of each class. (**J-L**) The statistical analysis of durotaxis-related parameters, including Forward Migration Index (FMI), persistence, and velocity of embryo migration on stiffness gradient substrates over 1.5 h treated with control or AACOCF3, n = 12. All box-and-whisker plots show the medians, maxima, minima, upper quartiles, and lower quartiles. * $p < 0.05$, ** $p < 0.01$, *** $p < 0.001$, **** $p < 0.0001$.

Figure 5

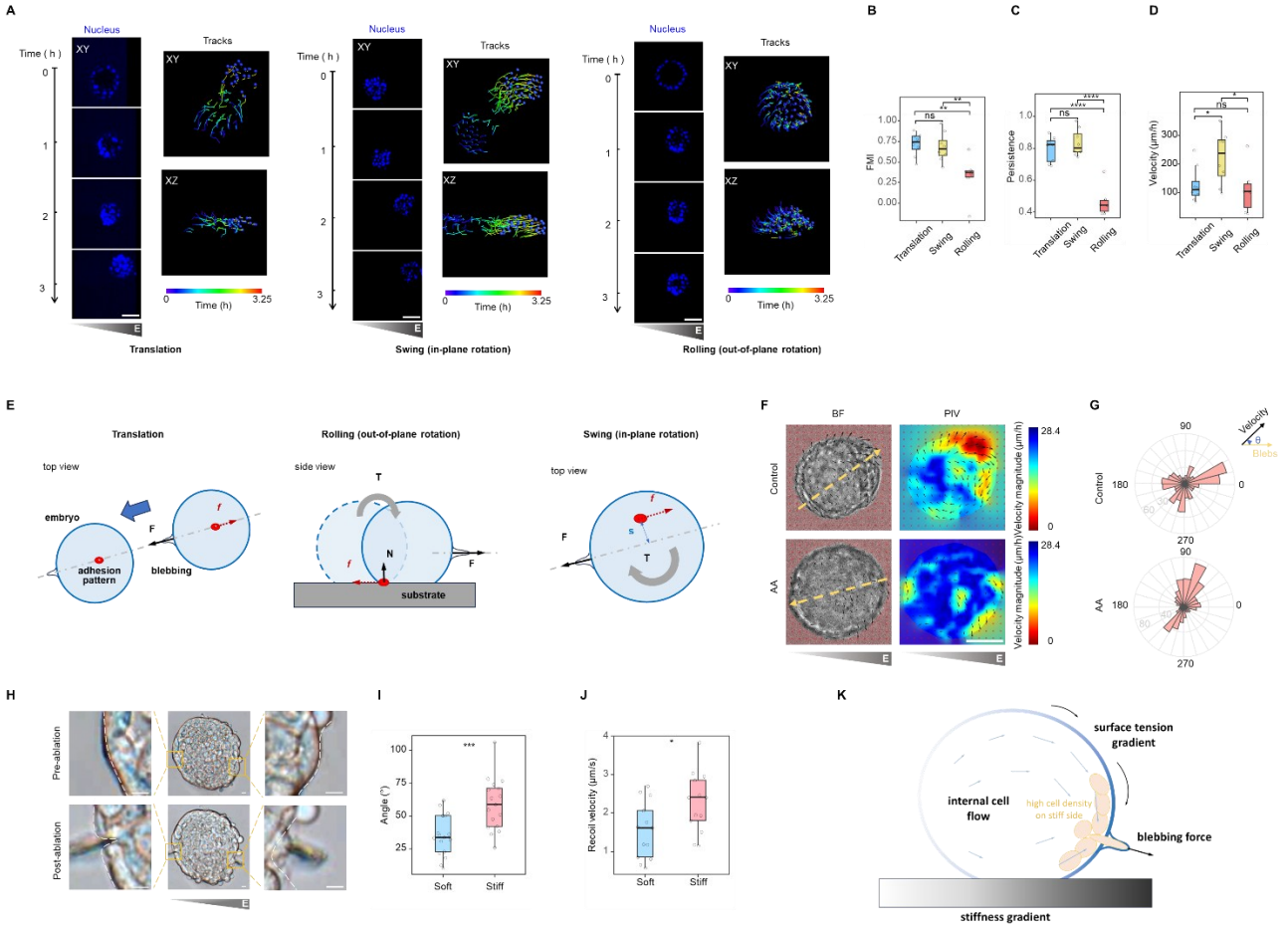

Figure 5. Multiple migration modes of embryo durotaxis driven by blebbing forces and a Marangoni-like flow mechanism. (**A**) Representative fluorescent images and spatiotemporal trajectory of cell nuclei labeled by SPY555 during embryo durotaxis on stiffness gradient substrates. Scale bar: 50 μm. (**B-D**) The statistical analysis of durotaxis-related parameters, including Forward Migration Index (FMI), persistence, and velocity of three embryo migration modes on stiffness gradient substrates over 3.25 h, n = 8. (**E**) Schematic diagram of force analysis on embryos under three migration modes. (**F**) Representative velocity field of embryos treated with control or AACOCF3 during embryo durotaxis on stiffness gradient substrates. Scale bar: 50 μm. (**G**) Rose diagram displays the angular between velocity field and cellular blebs in embryos treated with control or AACOCF3 during embryo durotaxis on stiffness gradient substrates. (**H**) Representative bright field images of embryos surface before and after UV laser ablation. Scale bar, 7 μm. (**I**) The opening angle after UV laser ablation in soft and stiff sides of embryo surface, n = 16. (**J**) The The cavity recoil speed after UV laser ablation in soft and stiff sides of embryo surface, n = 13. (**K**) Schematic diagram of a

Marangoni-like flow mechanism mediating embryo durotaxis driven by cell blebbing. All box-and-whisker plots show the medians, maxima, minima, upper quartiles, and lower quartiles. * $p < 0.05$, ** $p < 0.01$, *** $p < 0.001$, **** $p < 0.0001$.

Figure 6

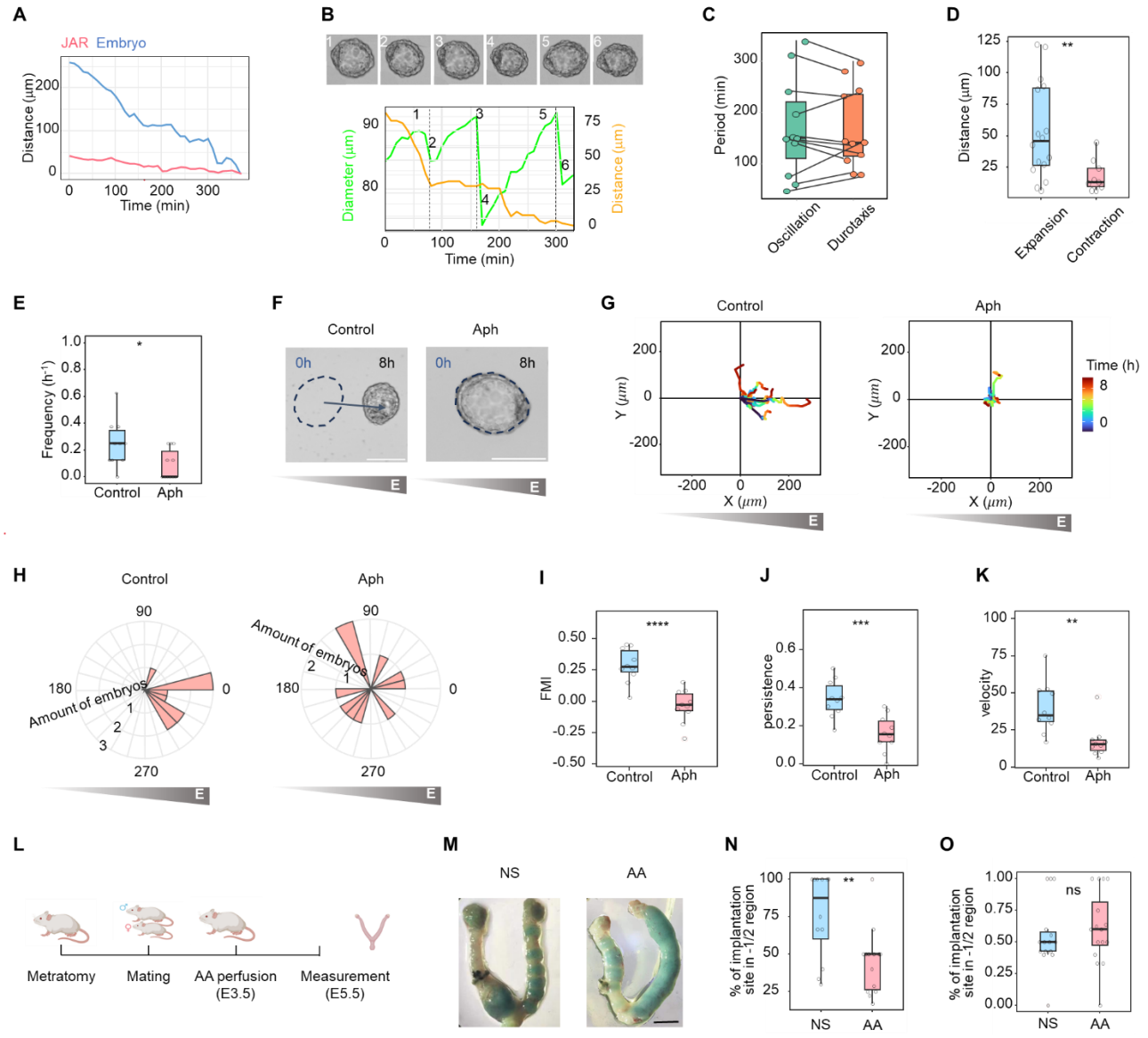

Figure 6. Durotaxis of mouse embryos exhibits periodicity and contributes to CSP pathogenesis. (**A**) The relationship between the distance to the endpoint and migration time during durotaxis of a JAR spheroid or a mouse embryo. (**B**) The relationships between the distance to the endpoint and migration time or the embryo diameter and migration time during durotaxis of a mouse embryo. (**C**) The statistical analysis of period duration in embryo oscillation or durotaxis, n = 11. (**D**) The statistical analysis of migration length in expansion phase or contraction phase in a single oscillation period, n = 16. (**E**) Oscillation frequency of embryos treated with control or aphidicolin, n = 10 (control), 11 (Aph). (**F**) Representative time-lapse images of embryos on stiffness gradient substrates treated with control

or aphidicolin. Scale bar: 50 μm. (**G**) Migration plots on gradient substrates over 12 h in embryos treated with control or aphidicolin. (**H**) Rose diagram of migration direction on substrates with gradient stiffness in embryos treated with control or aphidicolin, which displays the angular between migration and stiffness gradient and the frequency of each class. (**I-K**) The statistical analysis of durotaxis-related parameters, including Forward Migration Index (FMI), persistence, and velocity of embryo migration on stiffness gradient substrates over 1.5 h treated with control or AACOCF3, n = 10. (**L**) Schematic illustration of AACOCF3 perfusion treatment in pregnant mice uterine scar model. (**M**) The image of implantation sites in murine uterine scar model treated with control (normal Saline, NS) or AACOCF3. Scale bar: 5 mm. (**N**) The statistical analysis of implantation site percentage in -1/2 region at scar side of murine uterine scar model treated with control (normal Saline, NS) or AACOCF3, n = 12. (**O**) The statistical analysis of implantation site percentage at healthy side of murine uterine scar model treated with control (normal Saline, NS) or AACOCF3, n = 16. All box-and-whisker plots show the medians, maxima, minima, upper quartiles, and lower quartiles. * $p < 0.05$, ** $p < 0.01$, *** $p < 0.001$, **** $p < 0.0001$.

SUPPLEMENTAL FIGURES

Fig. S1.

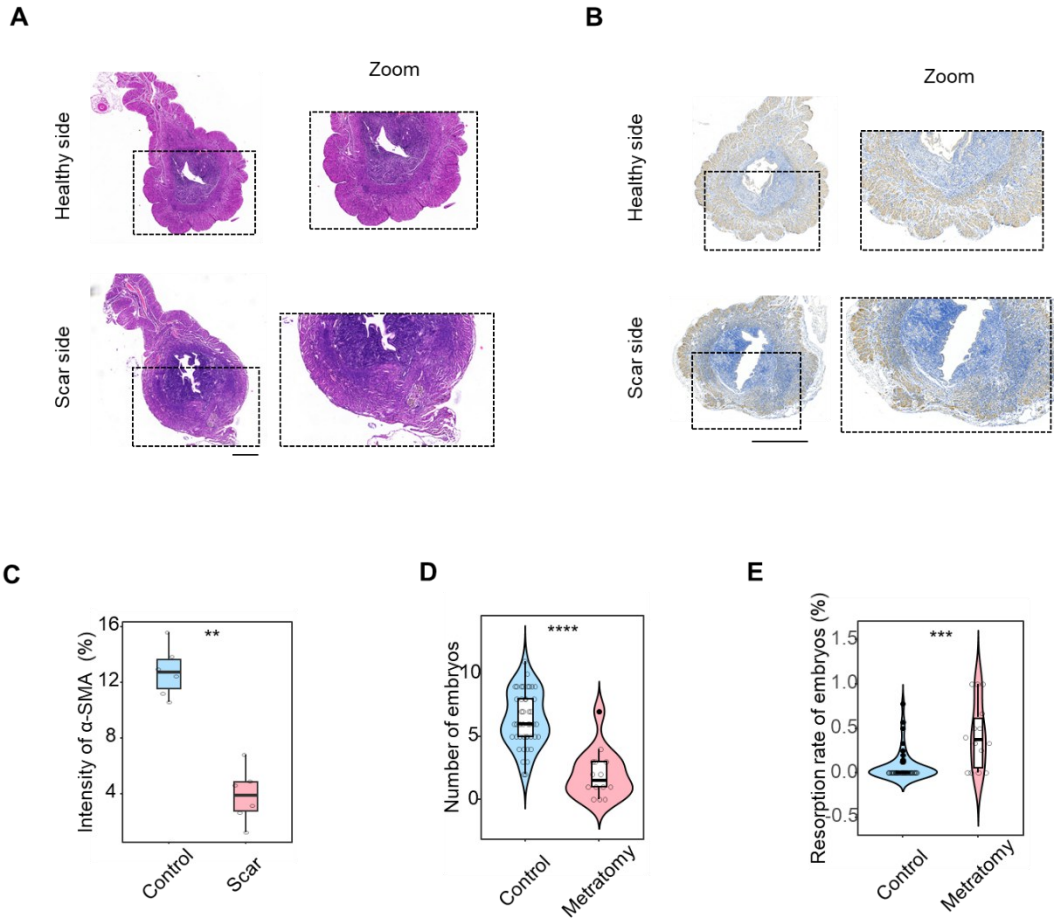

Fig. S1. Histological analysis of murine uterine scar model. (**A**) Representative images of HE staining in murine uterine scar model. Scale bar: 500 μm. (**B**) Representative images of immunohistology analysis of α−SMA in a murine uterine scar model. Scale bar: 800 μm. (**C**) Quantification of α−SMA intensity in the myometrium of the antimesometrial side or scar area. (**D**) The statistical analysis of embryo number at E7.5 stage in mice with metratomy or control mice, n = 44 (control), 14 (metratomy). (**E**) The statistical analysis of embryo resorption rate in mice with metratomy or control mice, n = 44 (control), 14 (metratomy). * $p < 0.05$, ** $p < 0.01$, *** $p < 0.001$, **** $p < 0.0001$

Fig. S2.

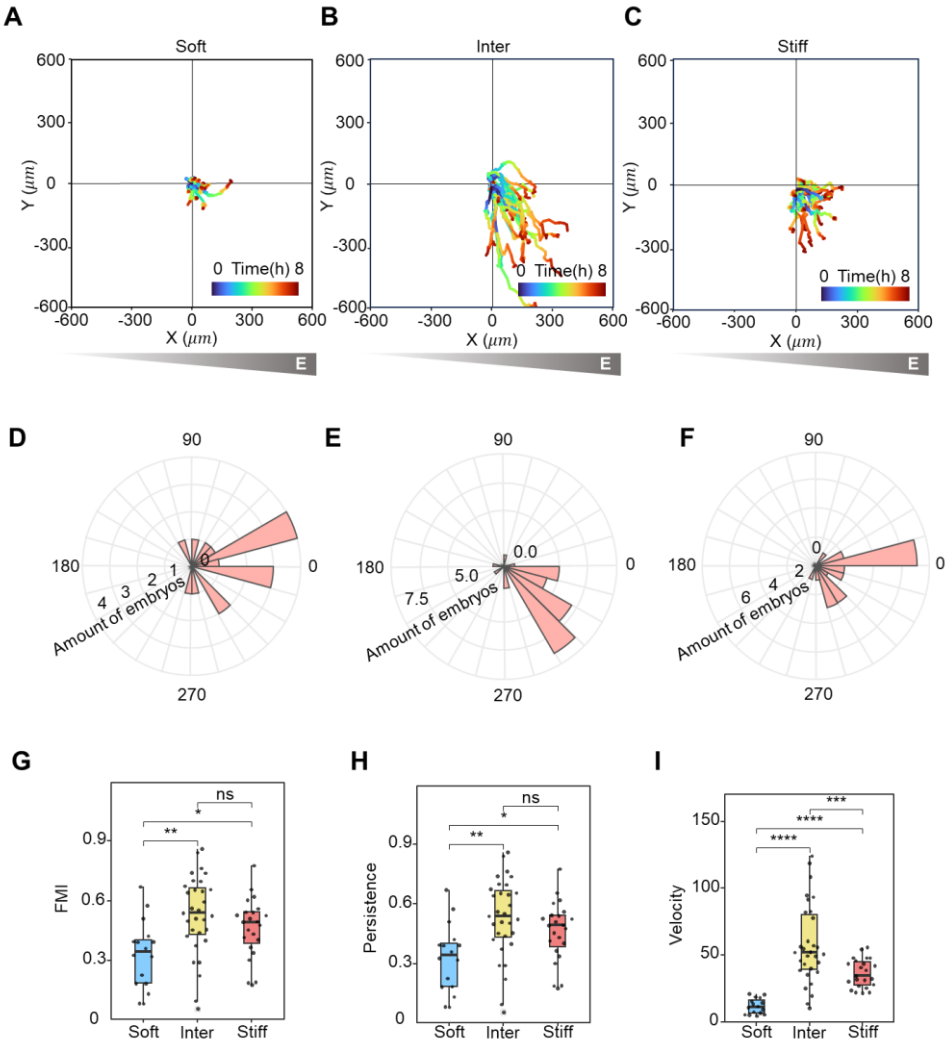

Fig. S2. Embryo durotaxis on substrates with gradient stiffness at different stiffness zones. (**A-C**) Embryo migration plots on gradient substrates over 8 h on substrates with gradient stiffness at different stiffness zones. (**D-F**) Rose diagram of embryo migration direction on substrates with gradient stiffness at different stiffness zones, which displays the angular between migration and stiffness gradient and the frequency of each class. (**G-I**) The statistical analysis of durotaxis-related parameters, including Forward Migration Index (FMI), persistence, and velocity of embryo migration on substrates with gradient stiffness at different stiffness zones. All box-and-whisker plots show the medians, maxima, minima, upper quartiles, and lower quartiles, n = 16 (soft), 31 (inter), 23 (stiff). * $p < 0.05$, ** $p < 0.01$, *** $p < 0.001$, **** $p < 0.0001$.

Fig. S3.

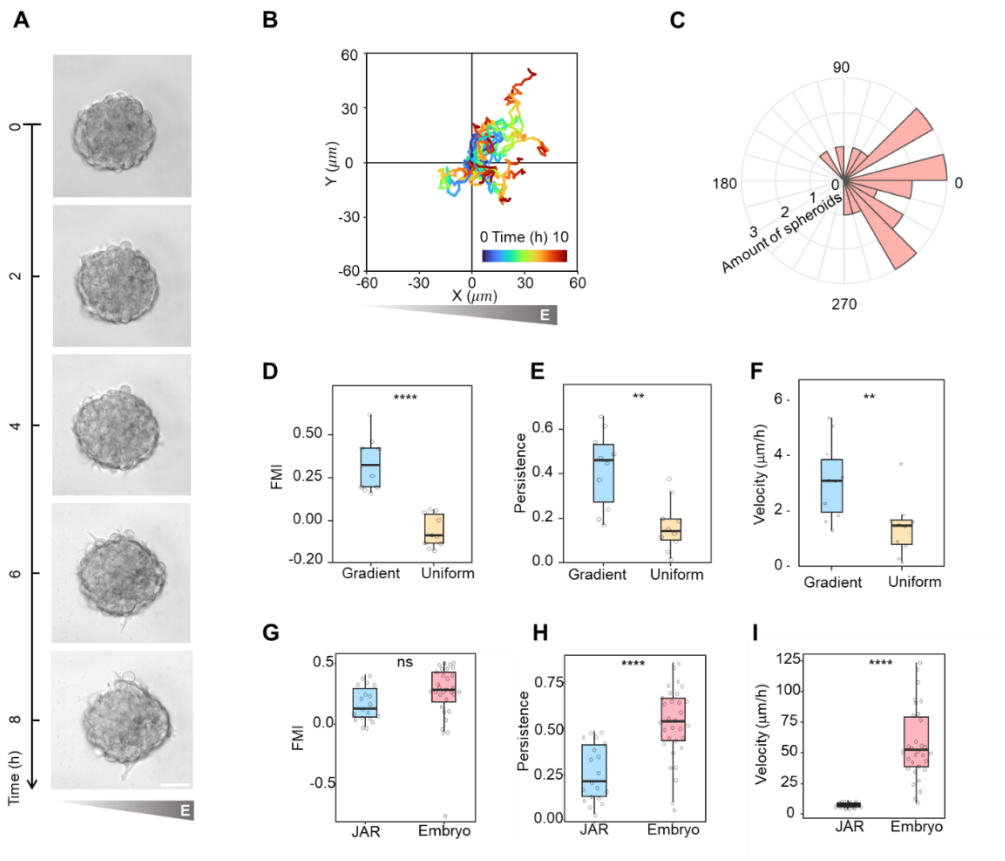

Fig. S3. Durotaxis of human trophoblast cell spheroids. (**A**) Representative time-lapse images of JAR spheroid on substrates with uniform stiffness or gradient stiffness. Scale bar: 20 μm. (**B**) JAR spheroid migration plots on gradient substrates over 10 h. (**C**) Rose diagram of JAR spheroid migration direction on substrates with uniform stiffness or gradient stiffness, which displays the angular between migration and stiffness gradient and the frequency of each class. (**D-F**) The statistical analysis of durotaxis-related parameters, including Forward Migration Index (FMI), persistence, and velocity of JAR spheroid migration on substrates with uniform stiffness or gradient stiffness, n = 9. (**G-I**) The statistical analysis of durotaxis-related parameters, including Forward Migration Index (FMI), persistence, and velocity of JAR spheroid or embryo migration on substrates with uniform stiffness or gradient stiffness, n = 19. All box-and-whisker plots show the medians, maxima, minima, upper quartiles, and lower quartiles. * $p < 0.05$, ** $p < 0.01$, *** $p < 0.001$, **** $p < 0.0001$.

Fig. S4.

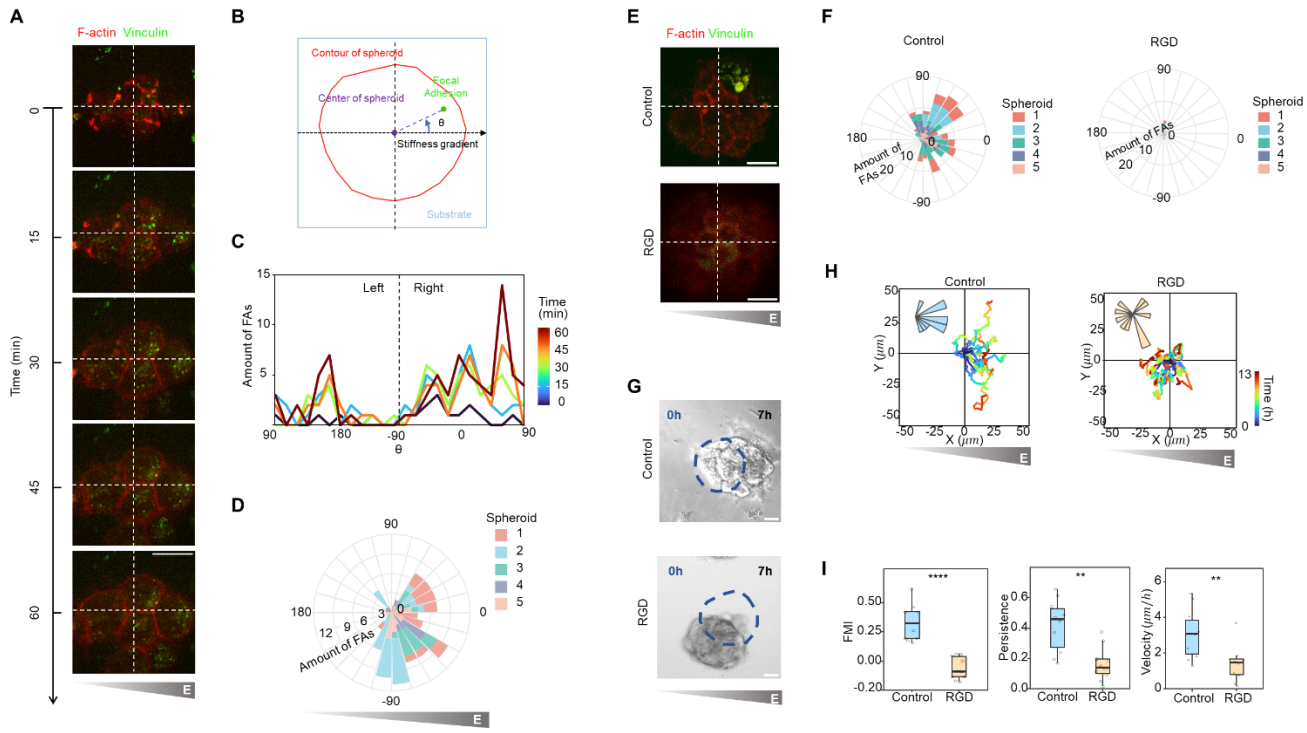

Fig. S4. The establishment of an asymmetric cell-substrate adhesion pattern is required for durotaxis of human trophoblast cell spheroids. (**A**) Representative time-lapse fluorescent images of Vinculin-GFP and Lifeact-mCherry signals at the spheroid-substrate interface in Vinculin-GFP^{+}/Lifeact-mCherry^{+} JAR spheroids. Scale bar: 20 μm. (**B**) Schematic illustration of angles (θ) between membrane signal related to spheroid center and substrate stiffness gradient. (**C**) The Vinculin-GFP intensity at the spheroid-substrate interface in Vinculin-GFP^{+}/Lifeact-mCherry^{+} JAR spheroids at different angles (θ) during the adhesion of spheroids to substrates. (**D**) Rose diagram of Vinculin-GFP signals at the spheroid-substrate interface in Vinculin-GFP^{+}/Lifeact-mCherry^{+} JAR spheroids, which displays angles (θ) between Vinculin-GFP signal related to spheroid center and substrate stiffness gradient. (**E**) Representative time-lapse fluorescent images of Vinculin-GFP and Lifeact-mCherry signals at the spheroid-substrate interface in Vinculin-GFP^{+}/Lifeact-mCherry^{+} JAR spheroids treated with control or RGD. Scale bar: 20 μm. (**F**) Rose diagram of Vinculin-GFP signals at the spheroid-substrate interface in Vinculin-GFP^{+}/Lifeact-mCherry^{+} JAR spheroids treated with control or RGD, which displays angles (θ) between Vinculin-GFP signal related to spheroid center and substrate stiffness gradient. (**G**) Representative time-lapse images of JAR spheroids on stiffness gradient substrates treated with control or RGD. Scale bar: 20 μm. (**H**) JAR spheroid migration plots on stiffness gradient substrates over 7 h treated with control or RGD. Insets are rose diagram of spheroid migration direction, which displays the angular between migration and stiffness gradient and the frequency of each class. (**I**) The statistical analysis of durotaxis-related parameters, including Forward Migration

Index (FMI), persistence, and velocity of JAR spheroid migration on stiffness gradient substrates over 7 h treated with control or RGD, n = 10 (control), 9 (RGD). All box-and-whisker plots show the medians, maxima, minima, upper quartiles, and lower quartiles. * $p < 0.05$, ** $p < 0.01$, *** $p < 0.001$, **** $p < 0.0001$.

Fig. S5.

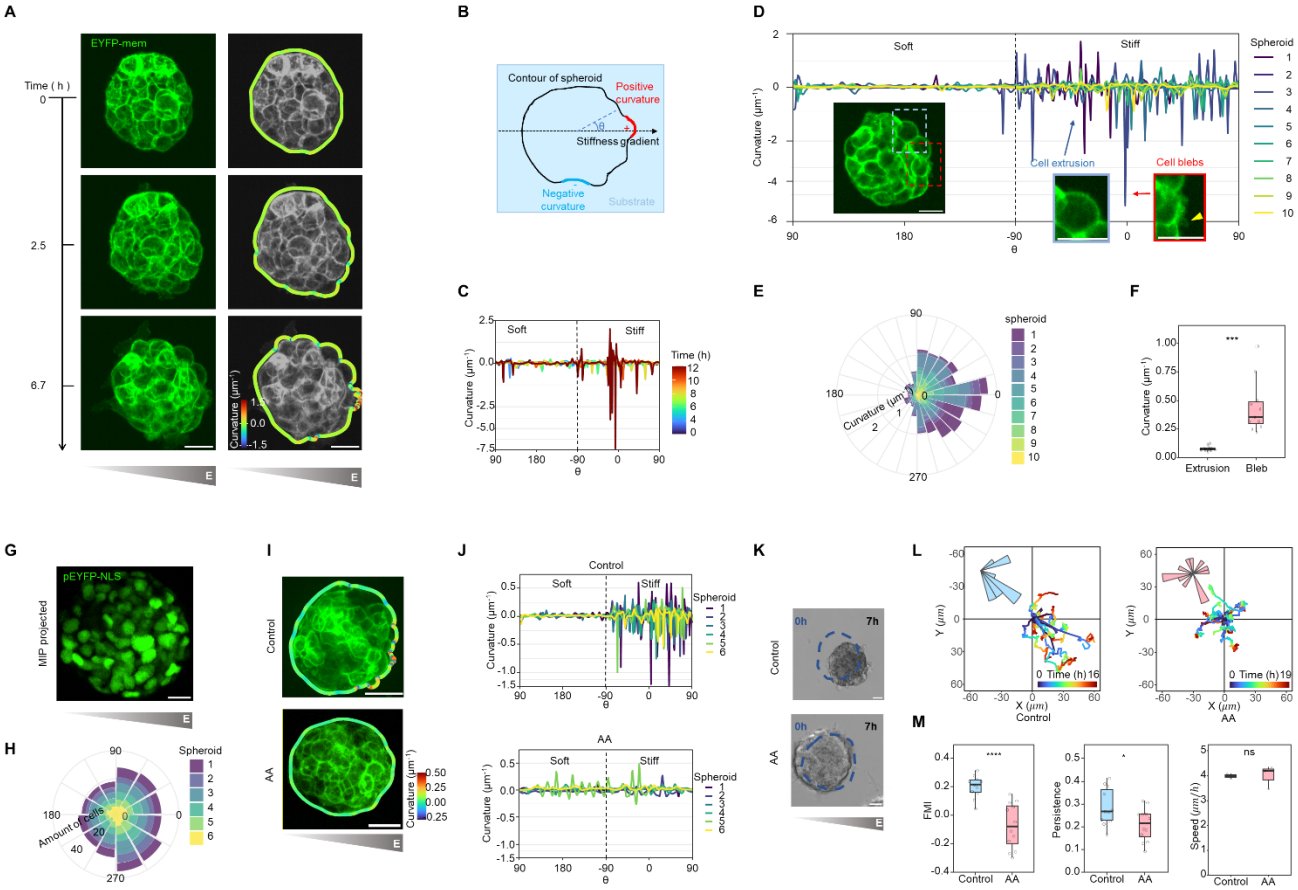

Fig. S5. Inhibiting cell blebbing disrupts durotaxis of human trophoblast cell spheroids. (**A**) Representative time-lapse images of surface morphology in EYFP-mem^{+} JAR spheroids over time on substrates with gradient stiffness. Scale bar: 20 μm. (**B**) Schematic illustration of angles (θ) between membrane signal to spheroid center and substrate stiffness gradient. (**C**) The surface curvature of JAR spheroids at different angles (θ) over time on substrates with gradient stiffness. (**D**) The surface curvature of JAR spheroids at different angles (θ) on substrates with uniform stiffness or gradient stiffness. Insets are presentative fluorescent images of EYFP-mem^{+} JAR spheroids with two distinct types of surface fluctuations. Scale bar: 20 μm. (**E**) Rose diagram of surface curvature of JAR spheroids, which displays angles (θ) between membrane signal related to spheroid center and substrate stiffness gradient. (**F**) The statistical analysis of curvature in two distinct types of cell extrusion and cellular blebs. (**G**) Representative fluorescent images of cell nuclei in EGFP-NLS^{+} JAR spheroids during durotaxis on stiffness gradient substrates. Scale bar: 20 μm. (**H**) The cell density at different angles (θ) on substrates with gradient stiffness. (**I**) The analysis of JAR spheroid surface curvature on stiffness gradient substrates treated with control or AACOCF3. Scale bar: 20 μm. (**J**) The surface curvature of JAR spheroids at different angles (θ) on stiffness gradient substrates treated with control

or AACOCF3. (**K**) Representative time-lapse images of JAR spheroids on stiffness gradient substrates treated with control or AACOCF3. Scale bar: 20 μm. (**L**) JAR spheroid migration plots on stiffness gradient substrates over 7 h treated with control or AACOCF3. Insets are rose diagram of spheroid migration direction, which displays the angular between migration and stiffness gradient and the frequency of each class. (**M**) The statistical analysis of durotaxis-related parameters, including Forward Migration Index (FMI), persistence, and velocity of JAR spheroid migration on stiffness gradient substrates over 7 h treated with control or AACOCF3, n = 11 (control), 12 (AA). All box-and-whisker plots show the medians, maxima, minima, upper quartiles, and lower quartiles. * $p < 0.05$, ** $p < 0.01$, *** $p < 0.001$, **** $p < 0.0001$.